An Improved Radio Frequency Interference Model: Reevaluation of the Kurtosis Detection Algorithm Performance Under Central-Limit Conditions

Sidharth Misra, *Member, IEEE*, Roger D. De Roo, *Member, IEEE*, and Christopher S. Ruf, *Fellow, IEEE*

***Abstract*—Recent airborne field campaigns making passive microwave measurements have observed some radio frequency interference (RFI) that remained undetected by the kurtosis RFI-detection algorithm. The current pulsed-sinusoidal model for RFI does not explain this anomalous behavior of the detection algorithm. In this paper, a new RFI model is developed that takes into account multiple RFI sources within an antenna footprint. The performance of the kurtosis algorithm with the new model is evaluated. The behavior of the kurtosis detection algorithm under central-limit conditions due to multiple sources is experimentally verified. The new RFI model offers a plausible explanation for the lack of detection by the kurtosis algorithm of the RFI otherwise observed.**

***Index Terms*—Central limit, microwave radiometry, radio frequency interference (RFI).**

I. Introduction

In RECENT years, passive spaceborne microwave remote-sensing measurements have been adversely affected by man-made radio frequency interference (RFI) sources [1], [2]. Measurements made in the C-, X-, and K-bands have all been affected by RFI [3]–[5]. Interference has been observed even in the protected 21-cm hydrogen line (L-band) from airborne and spaceborne campaigns [6]–[10]. Some RFI sources are high-powered spikes that can be easily detected and eliminated. Other RFI sources have low power, similar to the noise equivalent delta temperature (NEΔT) level of the measuring radiometer, and remain undetected. NEΔT represents the radiometric uncertainty in the measurements. If left unmitigated, the resulting Tb values can cause erroneous estimates of geophysical parameters.

In order to deal with such RFI, various missions have implemented detection algorithms. The Aquarius mission, launched in June 2011, oversamples the incoming thermal emission in order to temporally detect RFI outliers [11]. The soil moisture active passive (SMAP) mission, a high-priority mission identified in the recent National Research Council Earth decadal survey [12], is implementing as one of its RFI-detection option a statistical detection technique which measures the deviation from normality of the incoming thermal emission [13]. SMAP also spectrally divides the incoming signal into frequency bins to aid in isolating narrow-band RFI. The ability of the kurtosis algorithm to detect RFI around the NEΔT level of the radiometer has been successfully demonstrated in many field campaigns [8]–[10], [14]. In addition to the previously discussed algorithms implemented for these spaceborne missions, other RFI-detection algorithms have been developed such as the cross-frequency algorithm with fine spectral resolution [15] and spatial detection algorithms [16] that detect outliers among spatial pixels.

The performance analysis of most of the algorithms developed assumes a single pulsed-sinusoidal model for RFI [2]–[5], [10], where a pulse duty cycle of 100% represents a continuous-wave (CW) source. This model might not be valid for spaceborne missions. Spaceborne radiometers fly at higher altitudes than airborne instruments do, resulting in a larger antenna footprint and thus increased potential for multiple RFI sources affecting the signal. In the case of the kurtosis detection algorithm, multiple sources can cause the probability distribution of the incoming signal to tend toward a normal distribution due to the central-limit theorem. This can affect the ability of the kurtosis detection algorithm to detect RFI. A few obvious RFI spikes observed in airborne data have been missed by the kurtosis detection algorithm [31]. A new RFI model is proposed to explain the anomalous behavior of the detection algorithm.

This paper builds upon previous work by the authors in [17], adding detailed derivation and experimental verification, as well as field-campaign results supporting the RFI-model assumptions. The next section presents results from an L-band airborne campaign, SMAP validation experiment (SMAPVEX), performed using the University of Michigan's digital backend hardware. The detection algorithms are summarized in Section II, and the statistics of RFI missed by the kurtosis detection algorithm are presented. The new RFI model is detailed in Section III. The performance of the kurtosis detection algorithm under central-limit conditions is evaluated in Section IV, with experimental verification of simulation results presented in Section V. The last section summarizes this paper.

Manuscript received April 19, 2011; revised December 5, 2011; accepted February 11, 2012. Date of publication May 9, 2012; date of current version October 24, 2012. This work was supported in part by the National Aeronautics and Space Administration (NASA) under the NASA Earth and Space Science Fellowship (NNX08AU76H).

S. Misra is with the Microwave System Technology group, Jet Propulsion Laboratory, Pasadena, CA 91109 USA (e-mail: sidharth.misra@jpl.nasa.gov).

R. D. De Roo is with the Department of Atmospheric, Oceanic and Space Sciences, University of Michigan, Ann Arbor, MI 48109 (e-mail: deroo@umich.edu).

C. S. Ruf is with the Department of Atmospheric, Oceanic and Space Sciences and the Space Physics Research Laboratory, University of Michigan, Ann Arbor, MI 48109 USA (e-mail: cruf@umich.edu).

Color versions of one or more of the figures in this paper are available online at http://ieeexplore.ieee.org.

Digital Object Identifier 10.1109/TGRS.2012.2191972

0196-2892/$31.00 © 2012 IEEE

II. Hardware and Campaign Results

A. ADD Hardware

The University of Michigan's agile digital detector (ADD) was one of the three radiometer back ends that were integrated with the Jet Propulsion Laboratory passive/active L-/S-band (PALS) combined radar and radiometer [18] for flights on board a Twin Otter from September 22 to October 19, 2008. The other two back ends were the L-Band Interference Suppressing Radiometer [19] and the Analog Double Detector [20]. The Twin Otter SMAPVEX campaign involved transit flights between Grand Junction, Colorado, and Wilmington, Delaware; numerous soil-moisture science flights near Des Moines, Iowa, and Choptank, Maryland; and several RFI-specific flights near New York City, Atlanta, and elsewhere. RFI-related measurements were also performed by ADD during all transit and science flights.

ADD is a radiometer-back-end digitization and digital-signal-processing subsystem. Its input signals are vertical- and horizontal-polarization IF versions of the predetected radiometer signal. The signals are synchronously digitized with an 8 bit precision at slightly higher than the Nyquist rate for their bandwidth. The vertical- and horizontal-polarization signals are then passed through eight-channel digital subband filters, after which the V- and H-pol signals in each subband are cross correlated for Stokes vector recovery. The kurtosis of each individual V- and H-pol subband signal is also computed for the purpose of RFI detection. In addition, full-band versions of the V- and H-pol signals are also cross correlated, and each of their kurtosis values is also computed.

In the case of integration with PALS, the IF-signal output by PALS is centered at 200 MHz and has a 24-MHz bandwidth. The maximum analog frequency of the version of ADD that was flown with PALS was less than 200 MHz, so an additional demodulation stage was added which mixed the IF signal to a second IF signal centered at 27 MHz. The second IF signal was then digitized at 110 MHz.

B. Detection Algorithms

The kurtosis RFI detector identifies RFI in the amplitude or statistical domain by measuring the higher order moments of the incoming predetected voltage signal from a radiometer [10]. Kurtosis detection consists of flagging integration periods for which the deviation of the kurtosis (ratio of fourth central moment over the square of the second central moment) from its nominal RFI-free value is statistically significant. The threshold for significance is set at three times the standard error in the individual estimates of the kurtosis (the so-called NEΔK). The detection algorithm is independent of the incoming power, hence Tb variations, and is an effective tool for detecting low-level RFI compared to other detection algorithms [21]. Studies on the kurtosis statistic have found the algorithm to be extremely sensitive to low-duty-cycle pulsed RFI and less sensitive to CW-type RFI [15], [22]. For pulsed-sinusoid-type RFI, the kurtosis detection algorithm has a blind spot for a 50%-duty-cycle signal and very little sensitivity to signals around a 50% duty cycle. Alternate higher order algorithms, e.g., [23], have been proposed to supplement the kurtosis algorithm.

The peak detection algorithm is a direct adaptation of the baseline algorithm for the Aquarius radiometer. The algorithm is essentially a local "glitch detector," which finds a local expected value for each sample by averaging nearby RFI-free samples and then flags that sample as contaminated by RFI if it differs significantly from that expected value. One important characteristic of a peak detection algorithm is the integration time of the raw samples on which it is based. For the ADD deployment with PALS reported here, that integration time is 4 ms. There are also a number of adjustable parameters in the algorithm which affect its false-alarm rate and probability of detection. The values used here are consistent with those recommended for the baseline Aquarius algorithm in [11].

C. Campaign Results and Kurtosis Detectability Issues

This subsection summarizes the RFI-detection results obtained using the kurtosis and peak detection algorithms. A combination of the peak and kurtosis detection algorithms was used as a "ground-truth" detection algorithm to which other types of detection algorithms were compared. Note that this "ground truth" should be expected to contain a small number of false alarms—integration periods flagged as containing RFIs that are actually RFI free. "Ground truth" can be considered to be a combination of the following three detection sets:

$$P = \{x_i | \kappa(x_i) > (3 + 3\sigma_k)\} \tag{1}$$

$$C = \{x_i | \kappa(x_i) < (3 - 3\sigma_k)\} \tag{2}$$

$$P_k = \{x_i | \rho(x_i) = 1\} \tag{3}$$

where x_i represents individual 4-ms integration periods of the ADD, $\kappa(x_i)$ is the kurtosis value of x_i, σ_k is the standard deviation of kurtosis (NEΔK), $\rho(x_i)$ is the peak-detection-algorithm flag ($1 =$ RFI present; $0 =$ RFI free), P represents the set of integration periods flagged as having pulsed-type RFI (duty cycle $< 50\%$) because the kurtosis is above three, C represents the set of integration periods flagged as having CW RFI (duty cycle $> 50\%$) because the kurtosis is below three, and P_k represents the set of integration periods flagged by the peak detection algorithm.

In order to detect different types of RFI, the following detection set is applied as "ground truth":

$$A = P \cup C \cup P_k. \tag{4}$$

It should be noted that "ground truth" does not contain weak RFI sources missed by both detection algorithms. Section IV briefly discusses such RFI sources. Comparing the kurtosis detection algorithm to "ground truth," we obtain RFI that was detected by the peak detection algorithm but not by the kurtosis algorithm. This is called blind/false RFI. Some of it could be RFI with a near-50% duty cycle with respect to the kurtosis integration time, to which the kurtosis algorithm is blind [10]. Some of it could be RFI from multiple sources (discussed in Section III), and some of it is apparently the result of a false alarm by the peak detection algorithm. Fig. 1 shows the

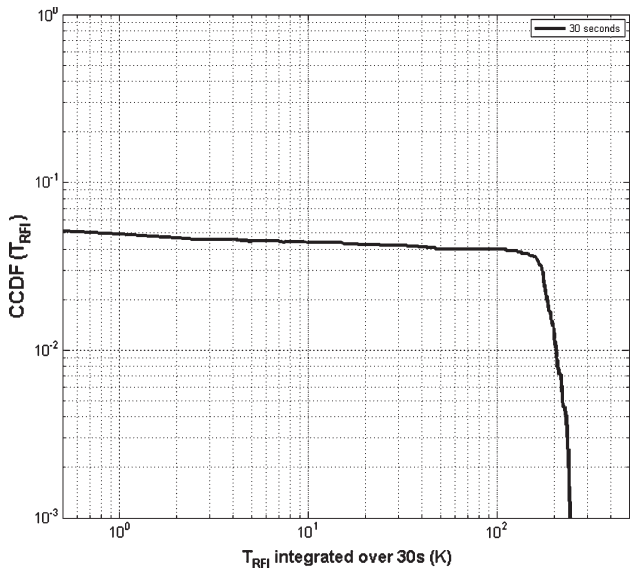


Fig. 1. CCDF $(= 1 - CDF)$ of the brightness-temperature contribution of blind RFI, i.e., RFI detected using the peak detection algorithm but not detected by kurtosis, integrated over 30 s.

complementary cumulative distribution function [(CCDF); $1 - CDF$] of blind/false RFI, measured by combining 4-ms integration periods into a 30-s period. It indicates the fraction of blind RFI present above the brightness temperature (Tb) shown on the x-axis. In other words, the y-axis of the plot indicates the fraction of total RFI missed by kurtosis but detected by pulse-detection algorithm, and the x-axis represents the minimum power of RFI sources which were undetected during the SMAPVEX campaign. The CCDF approaches unity as the RFI power approaches zero, as a result of a combination of false alarms by the pulse-detection algorithm or missed detections by the kurtosis algorithm as RFI levels approach zero. Where the CCDF is flat, no algorithm observed the RFI of that power. RFI under 0.5 K is not considered significant for retrievals such as soil moisture and is not shown in the figure.

The RFIs around the 100 K region are not false alarms and indicate RFI definitely missed by the kurtosis detection algorithm. The flat CCDF curve below the high RFI Tbs indicates that kurtosis is missing a few large RFI sources. The next few sections attempt to investigate the reason for such anomalous behavior of the kurtosis detection algorithm.

Fig. 2 gives an example of such isolated cases during the SMAPVEX campaign where the kurtosis detection algorithm has been unable to detect obvious high-power RFI. The blue curve in the figure shows raw 4-ms calibrated brightness without any RFI detection algorithm applied to it. The red curve only shows brightness temperatures that are considered to be RFI free after applying the kurtosis detection algorithm. As shown, most of the RFI is detected, yet some high-power RFI remains undetected, which can wash out and cause low-level errors if consecutive integration periods are averaged together. One possible explanation for these missed detects is that the offending RFI source has a perfect 50% duty cycle with respect to the radiometric integration time. However, the kurtosis statistic observed does not behave similar to a signal with a 50% duty cycle when integration periods are combined [24].

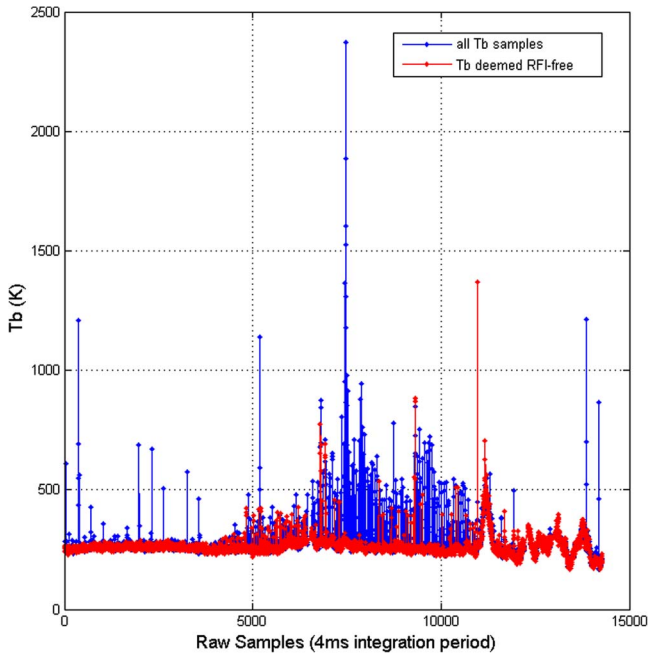


Fig. 2. Brightness-temperature values over New York City, indicating RFI [(blue) all Tb samples; (red) Tb deemed RFI free after applying full-band kurtosis algorithm], where each sample represents 4 ms.

III. Multiple-Source RFI Model

An alternative to considering the described kurtosis-detection anomalies as a 50% blind spot is to assume the possibility of multiple RFI sources within the antenna footprint. Previous literature [15], [21]–[23], [25] has modeled RFI as a single pulsed-sinusoidal source. This RFI model was originally valid for L-band sources since most RFI expected is of the pulsed type from air-defense and air-traffic control radars [7]. Recent experience from L-band airborne campaigns [8], as well as spaceborne missions such as soil moisture ocean salinity (SMOS), indicates that a large amount of in-band RFI exists that might not be radar sites. On the other hand, communication signals that exist at other frequencies such as C-, X-, and K-bands are mostly of CW nature (high duty-cycle), and multiple such sources might exist within the antenna footprint. Given the recent experience with this type of interference, a new RFI model must be developed to explain missed detections by the kurtosis algorithm. This new model can also be used for assessing the performance of other RFI-detection algorithms with respect to detectability of interference.

A more general RFI model is proposed which provides for the possibility of multiple pulsed-sinusoidal sources. It is given by

$$x(t) = n(t) + \sum_{i=1}^{N} A_i \cos(2\pi f_i t + \phi_i) \text{rect}\left(\frac{t - t_0}{w_i}\right), \quad t \in [0, T] \tag{5}$$

where $n(t) \sim N(0, \sigma^2)$ is normally distributed with zero mean and standard deviation σ, A is the amplitude of the RFI source, f is the frequency, ϕ is the phase shift, t_0 represents the center of the on pulse of the duty cycle, w is the width of the pulse,

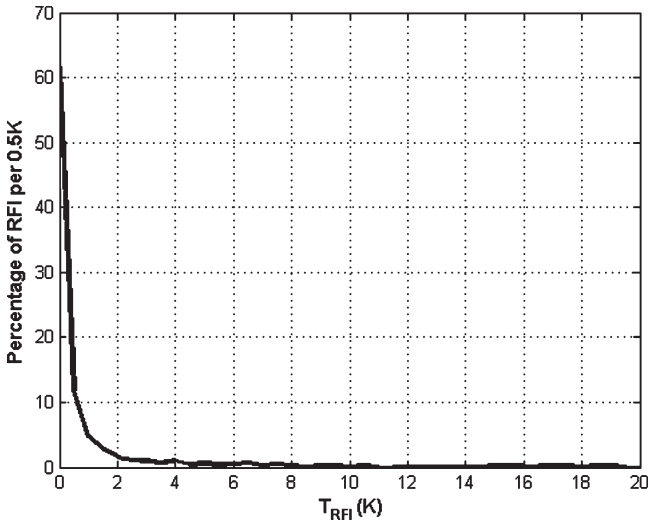


Fig. 3. Normalized distribution of RFI brightness temperature observed during the SMAPVEX campaign.

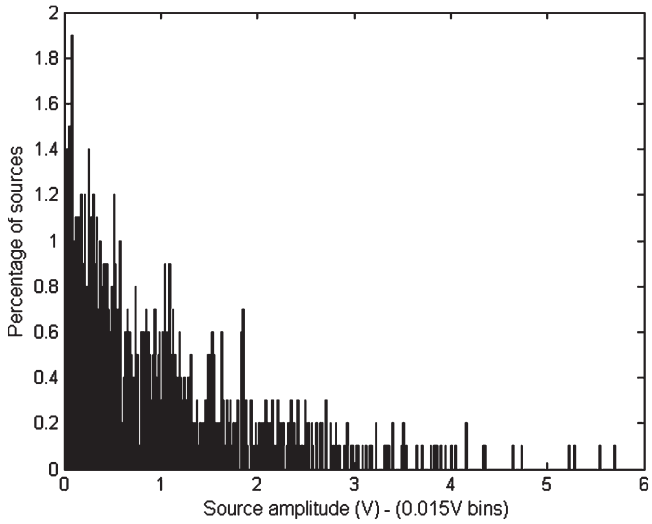


Fig. 4. Individual realization of the exponential pdf for the amplitude of individual RFI sources. The mean of the exponential pdf is a scalable parameter based on required output power. The above plot has a mean of 1 V.

and T is the integration period. The ratio $(d = w/T)$ represents the duty cycle of the RFI source. f is assumed to be uniformly distributed between [0, B] where B is the bandwidth of the radiometer. ϕ and t_0 are assumed to be uniformly distributed between [0, 2π] and [0, T], respectively. N is the total number of RFI sources.

The model described in (5) has two undetermined random variables associated with it: the amplitude A and the duty cycle d. Within an antenna footprint, it is expected that the various RFI sources would have a variety of power levels. In addition, the side lobes will see an RFI source differently than the main lobe of an antenna will. As a result, A is modeled as a random variable. In order to obtain characteristic data of a typical RFI amplitude distribution, the SMAPVEX campaign was used. Fig. 3 shows the distribution of RFI power observed during the campaign. RFI power is obtained by a two-step process: discarding RFI-affected samples as flagged by the "ground-truth" algorithm and combining the rest of the clean samples over a 30-s integration period. These clean samples are then subtracted from the original Tb samples also integrated to 30 s, to give the RFI Tb contribution. Fig. 3 shows the percent of total RFI present within 0.5 K bins from 0 to 20 K. As noted, the distribution is exponential in nature with mostly low-power RFI with a very few high-power sources as outliers. Assuming the SMAPVEX data are representative of general RFI characteristics, the amplitude probability density function (pdf) is given by

$$f(A) = \frac{1}{\upsilon} \exp(-A/\upsilon) \tag{6}$$

where $f()$ represents the pdf, A is the amplitude random variable of RFI, and ν is the mean of the exponential pdf. For simulation purposes, the exponential mean is scaled to match the total power contribution (sum of the distribution) between scenarios with different numbers of sources. Fig. 4 shows a typical realization of the amplitude pdf considered in this paper.

Similarly, it is expected that most RFI sources within an antenna footprint would have different duty cycles from each other. The relative occurrence of RFI with a pulsed or CW duty cycle can be characterized in a data set like that of the SMAPVEX campaign by noting whether the value of the kurtosis is above or below three.

In general, at L-band, RFI is mostly pulsed type in nature as noted from the SMAPVEX flight campaign and similar results confirmed by analysis in [21] and [26]. These are typical of L-band signals measured during airborne campaigns and may not apply to other microwave bands or spaceborne radiometers. SMOS has observed many RFI sources within L-band, but due to poor temporal resolution, SMOS cannot distinguish between a pulsed and a CW source. Communication signals exhibit CW behavior or have a high duty-cycle. Thus, we consider a bimodal pdf with respect to duty cycle, where the low duty-cycle region is approximated by a Rayleigh distribution, and the high duty-cycle region is approximated by an exponential distribution as

$$f(d) = p\left(\frac{d}{b_d^2}\exp\left(-\frac{d^2}{2b_d^2}\right)\right) + (1-p)\left(\frac{1}{\upsilon_d}\exp\left(-\frac{1-d}{\upsilon_d}\right)\right) \tag{7}$$

where $f()$ is the pdf, d is the duty-cycle (pulsewidth) random variable, p is the fraction of low duty-cycle sources, $1 - \nu_d$ is the mean of the exponential pdf, and b_d is the mode of the pdf. For simulation purposes, ν_d is kept around 0.1, and b_d is kept around 0.05. Both values are variable parameters that can be changed to assess the performance of detection algorithms. The Rayleigh distribution approximates a mostly low duty-cycle signal, whereas the decaying exponential pdf approximates signals around 100%-duty-cycle trailing off toward 50%. The fraction p is a variable parameter that controls the amount of low to high duty-cycle sources within a single footprint. Fig. 5 shows a duty-cycle pdf with an equal number of high- and low duty-cycle sources.

In order to calculate the kurtosis of a thermal signal corrupted by multiple pulsed-sinusoidal signals, it is necessary to obtain the pdf of the resulting signal. The previous RFI model [22],

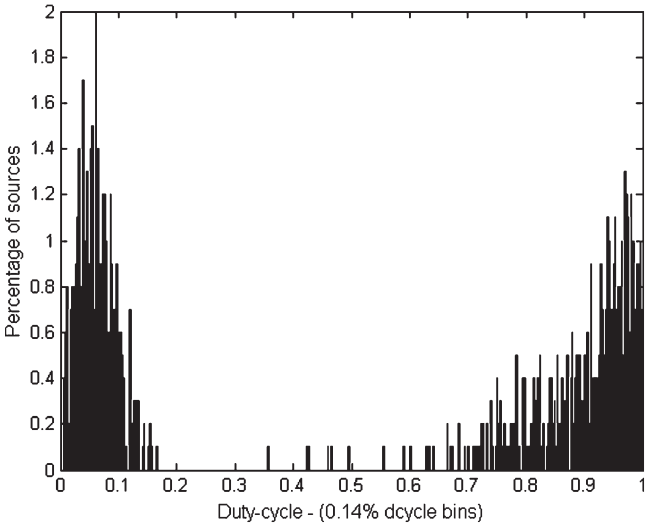


Fig. 5. Individual realization of the bimodal pdf applied for the duty cycle of individual RFI sources. The fraction of low duty-cycle to high duty-cycle is a variable parameter with the above plot indicating 50% of sources with low duty-cycle.

[23] used a pdf of a thermal-noise source with additive pulse-sinusoidal RFI obtained from [27]. It is difficult to obtain an elegant closed-form expression for such a pdf. Instead, the probability density is calculated using the characteristic function of the signal. The probability density of (5) is calculated in the Appendix and shown as follows:

$$f(t) = F^{-1}\left[e^{-\frac{\sigma^2 u^2}{2}} \prod_{i=1}^{N} (d_i J_0(A_i u) + (1 + d_i))\right] \quad (8)$$

where J_0 is a Bessel function of the zeroth order, A_i is the amplitude of the ith RFI source, d_i is the duty cycle of the ith RFI source, σ is the standard deviation of a normally distributed function, and $F^{-1}[\ldots]$ represents the inverse Fourier transform operation with respect to u.

Fig. 6 shows the pdf of a Gaussian signal corrupted by a single RFI source and multisource RFI. Note that these distributions will, in general, depend on various parameters such as mean power and duty-cycle fraction. Due to central-limit conditions, the pdf of a multisource corrupted thermal signal approaches a bell-shaped curve, similar to the uncorrupted original signal. This property is expected to impact the performance of the kurtosis detection algorithm with regard to detectability of RFI, which is investigated in the next section.

IV. Kurtosis Performance

The performance of the kurtosis detection algorithm can be assessed when multiple RFI sources are present within the antenna footprint. In order to account for the random distribution of duty cycle and amplitude of the RFI sources, Monte Carlo simulations were performed, and the average kurtosis and power were determined in each case. The total power contributed by all RFI sources is kept constant as the number of sources increases. An example is considered in which the total power level of RFI is nearly 100 times the NEΔT. Fig. 7 shows the value of the kurtosis ratio with respect to the number of sources and fraction of low duty-cycle sources within the antenna footprint. The orange region of the contour plot represents a kurtosis of approximately three, meaning that the amplitude pdf of the signal is either similar to Gaussian or, in some cases, a non-Gaussian pdf resulting in a kurtosis value of three (e.g., single RFI source of 50% duty cycle). The detection algorithm interprets this as a signal of geophysical origin, so if this is in fact RFI, it constitutes the blind-spot region for the detection algorithm. As can be seen in Fig. 7, with a large number of sources, the kurtosis becomes Gaussian-like. RFI sources with low duty-cycle sources converge toward three at a much slower rate than RFI sources with even a small fraction of CW sources. Kurtosis still maintains superior detectability for low duty-cycle sources, but the performance degrades rapidly due to the inclusion of communication-type CW signals. This indicates that the fraction of high duty-cycle sources dominates

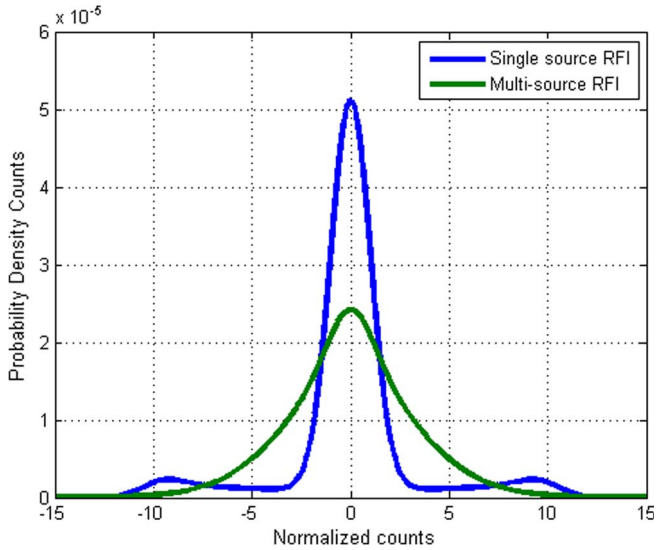


Fig. 6. PDF of RFI with thermal noise. The blue curve is for a single RFI source, and the green is for multiple sources, i.e., 50 sources, all of which have low duty-cycle. The relative RFI power of the different types of RFI sources is approximately ten times the thermal noise.

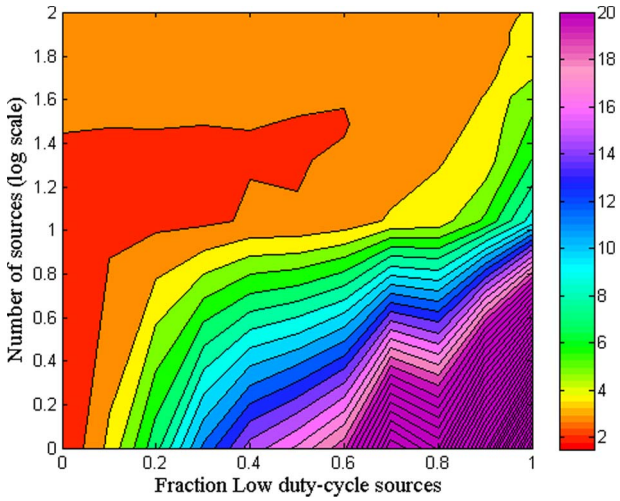


Fig. 7. Mean value of kurtosis as a function of the number of sources (1–100) and fraction of low duty-cycle sources. The overall power remains the same as the number of sources increases (orange $\rightarrow$ kurtosis $= 3$).

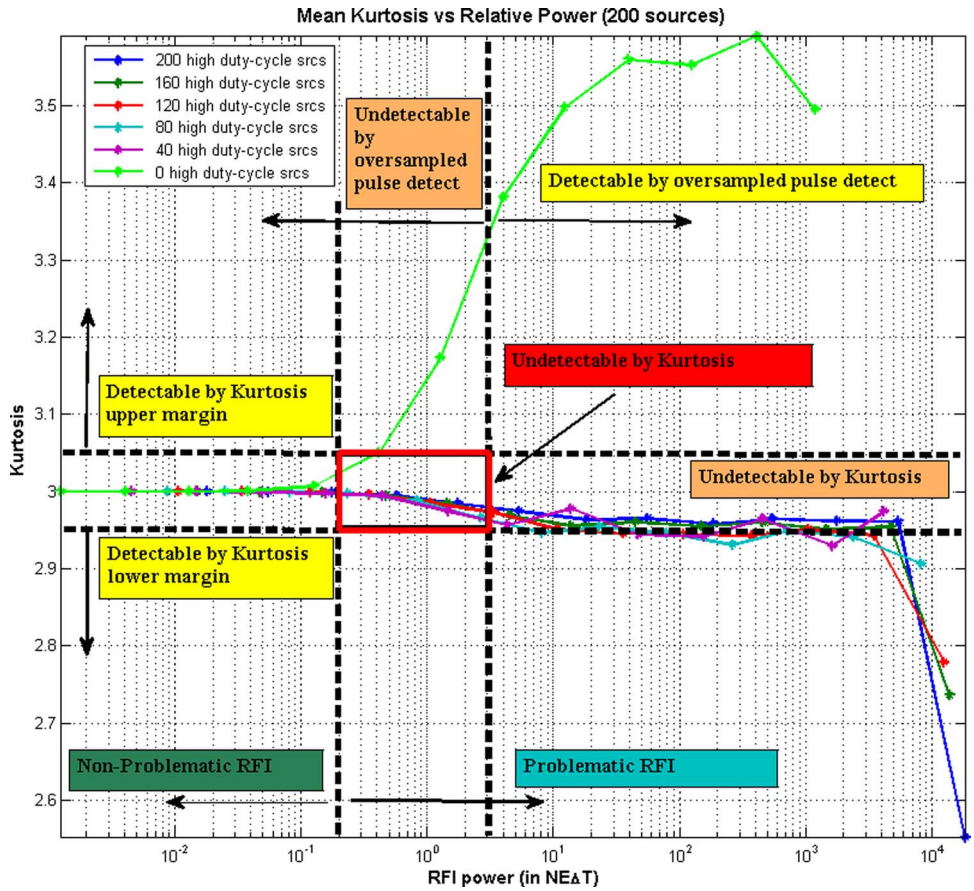


Fig. 8. Mean value of kurtosis versus RFI power (in NEΔT) for 200 sources [(region between black dashed lines) undetectable RFI by kurtosis or pulse detection; (red rectangle) undetectable problematic RFI].

the performance of the kurtosis detection algorithm. Similarly, for a low number of sources, the fraction of low duty-cycle sources dominates the performance of the kurtosis detection algorithm, whereas for a large number of sources, the impact of low duty-cycle signals is reduced.

Some field campaigns at L-band have shown RFI to be of a pulsed nature [21], [26], and kurtosis has high detectability for such RFI sources. Thus, several low duty-cycle sources in the L-band would need to be present for kurtosis to be affected by central-limit conditions. Also, a larger number of RFI sources results in a higher interference power. Some spaceborne radiometers such as SMAP plan to operate a hybrid of the kurtosis detector and pulse-detection algorithms that can easily identify large brightness-temperature jumps. Thus, the issue of central limit should not be a problem for SMAP because even if the kurtosis misses detecting such RFI, a large number of sources resulting in high-power RFI should be detected by the pulse-detection algorithm.

Detectability for SMAP will be an issue when the power is low enough for pulse detect to miss RFI but the number of sources is large enough for central-limit conditions to apply to the kurtosis. With the increasing popularity of low-power radio frequency identification device and wireless fidelity (Wi-Fi) systems operating on individual electronic devices, RFI corruption from such devices might not be in the form of an obvious spike (or jump) and might be low enough to be near the NEΔT of the radiometer. The kurtosis detector is capable of detecting spread-spectrum low-power systems [25], but with multiple sources and low power, detection becomes an issue. This is shown in Fig. 8. The figure shows the effect on kurtosis when observing 200 sources, as the relative power decreases. The different color curves represent different fractions of high duty-cycle sources within the total 200 sources. The red rectangular box indicates a region where RFI power is between 0.2 and 3 times the NEΔT and kurtosis is within three times the NEΔK, the detection threshold of kurtosis, assuming $\sim$100 K independent samples in an integration period. RFI within this box will be undetectable yet will have large-enough power (above 0.2 NEΔT) to be problematic and impact science measurements [28].

V. Experimental Verification

In order to demonstrate the performance of the kurtosis detector in the presence of multiple RFI sources, a bench-top radiometer experiment was performed. Fig. 9 shows a block diagram of the setup. The experimental setup uses a National Instruments arbitrary waveform generator (AWG) N8241 to simulate background microwave thermal emission with RFI corruption. The AWG operates at a sampling rate of 1.25 Gs/s. An inverse Fourier transform of a random spectrum populated according to Section III generated waveforms of phase-matched and filtered thermal noise with RFI from a varying number of sources.

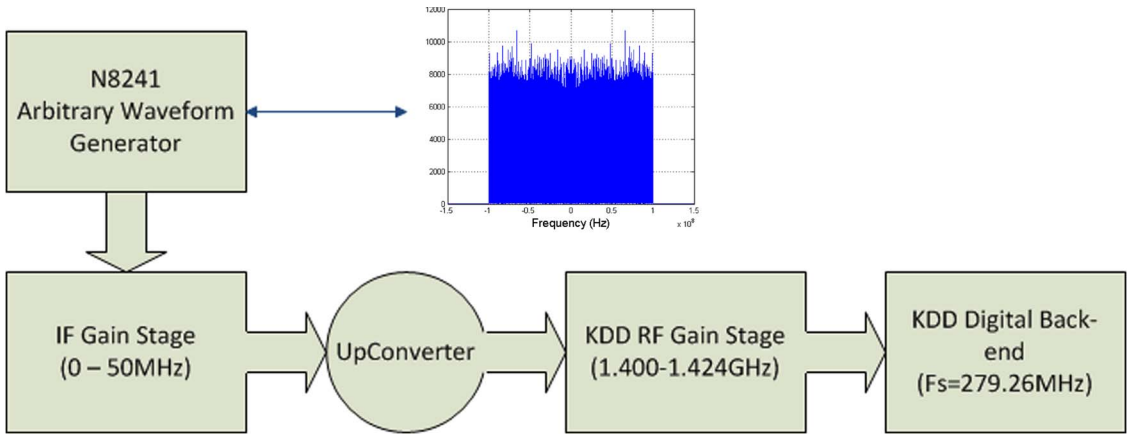


Fig. 9. Block diagram of Multisource RFI experimental setup.

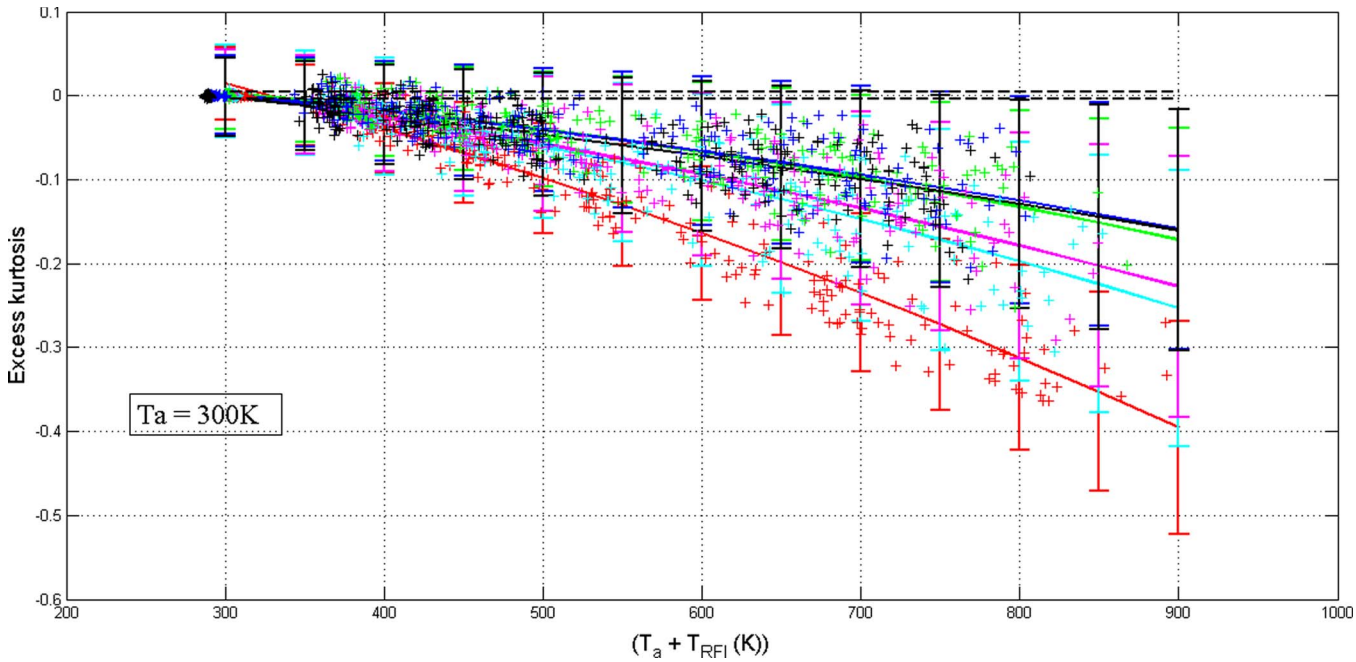


Fig. 10. Experimental results indicating excess kurtosis versus antenna Tbs in Kelvin (scaled assuming RFI-free thermal emission of $T_{\rm ant} = 300$ K). The dashed lines represent the $+/-3^*{\rm NE}\Delta K$ of kurtosis. The colors represent any RFI corruption due to different numbers of sources. The error bars represent the $1-\sigma$ confidence in the fit (number of sources: red $= 1$, cyan $= 3$, purple $= 5$, green $= 7$, blue $= 9$, and black $= 11$).

Analog signal output from the AWG (with a baseband bandwidth of 500 MHz) was then up converted to a 1.413 GHz center frequency and filtered between 1.4 and 1.424 GHz. The signal was then introduced into the University of Michigan kurtosis digital detector (KDD) RF stage and digital back end [29]. In summary, KDD subsamples the RF input signal at a rate of 279.26 MHz, after which digital signal processing is performed, including detection of the signal's kurtosis. For purposes of this experiment, band-limited Gaussian noise covered the spectral passband, and simulated RFI was uniformly distributed across the passband.

Fig. 10 shows results from the laboratory experiment, in which a background thermal source is corrupted with additive RFI. The overall relative power of the RFI was kept the same for a varying number of sources. The plot indicates excess kurtosis $(=$ kurtosis $-\ 3)$ versus RFI in scaled brightness-temperature units, based on a 300 K clean thermal background. All of the RFI sources have a high duty-cycle, which is why the excess kurtosis is below zero. Simulations from previous sections indicate that high duty-cycle sources have an immediate impact on kurtosis as the number of sources increases. As a result, the RFI sources with high duty-cycle were input through the AWG for verification purposes. The dashed lines represent the noise margin of kurtosis (i.e., $3^*{\rm NE}\Delta K$) for this system. Any integration period with excess kurtosis between the dashed lines has undetectable RFI. The colors in Fig. 10 represent different data points with the same number of RFI sources. For example, red represents data points with a single RFI source, and black represents 11 RFI sources. The other colors represent intermediate numbers of RFI sources. The experimental

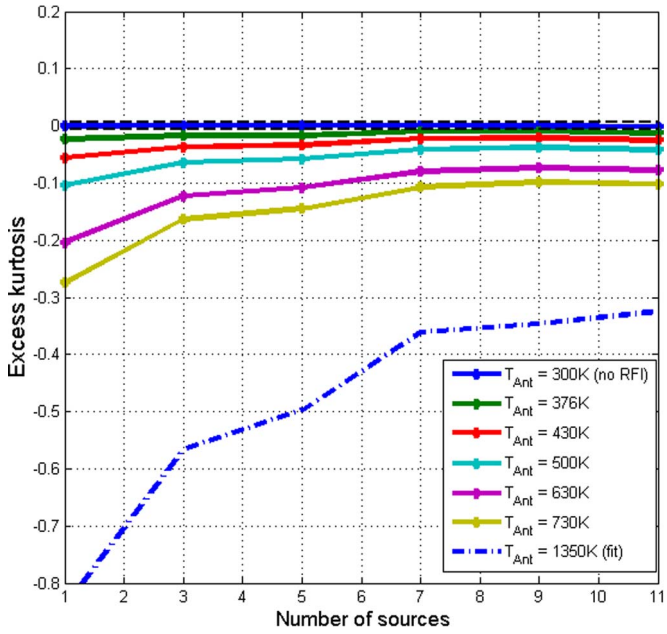


Fig. 11. Curves indicating kurtosis variation versus the number of RFI sources for different power levels. The solid lines represent mean kurtosis calculated from experimental data, and the dashed curve is fit from the experimental data at 1350 K Tb with a 300 K background.

results confirm that as the number of sources increases, the detectability of the kurtosis decreases. This is apparent by looking at the slope of the single-source high-duty-cycle RFI (red data), which is more negative, whereas for multiple-source high-duty-cycle RFI (e.g., black), the slope tends more toward the horizontal.

As an example, these results can be used to interpret and explain the presence of the large ($\sim$1350 K) RFI spike noted in Fig. 2 that was not identified by the kurtosis detector. If the antenna footprint for this integration period is assumed to contain multiple high duty-cycle RFI sources, the minimum number of sources required to cause an RFI spike of 1350 K that is blind to the kurtosis can be calculated. Performing a quadratic fit to the data in Fig. 10, it is possible to parameterize the behavior of kurtosis with respect to the number of sources for different power levels. It should be noted that the variance of excess kurtosis is larger with lesser number of sources, and the error bars in Fig. 10 indicate the $1-\sigma$ confidence of the quadratic fit. The curves in Fig. 11 indicate how the kurtosis approaches three (excess kurtosis $=0$) as the number of sources increases based on the quadratic mean fit of Fig. 10. Calculating a fitted curve for $T_{\rm ant}$ of 1350 K, it is found that, on average, approximately 27 separate high duty-cycle RFI sources are needed to cause such a spike to be missed by the kurtosis detector. If we consider curves based on the minimum and maximum $1-\sigma$ confidence fit, the number of such sources could be as low as 14 and as high as 40. The approximate result obtained from fitting the experimental data indicates a relatively low number of high duty-cycle RFI sources required to miss high-power RFI spikes. The geographic location of the antenna footprint for the 1350 KTb spike in Fig. 2 was latitude $=40.74^\circ$ N, longitude $=74.04^\circ$ W, which is approximately near Manhattan, New York City. Urban areas can be expected to contain a higher density of CW RFI emitters.

VI. Conclusion and Discussion

Recent airborne field campaigns such as SMAPVEX have observed some high-powered RFI events missed by the kurtosis detection algorithm. The current single pulsed-sinusoidal RFI model has failed to explain the anomalous behavior of the kurtosis detector. This has necessitated the development of a new RFI model. The new RFI model takes into account multiple sources within an antenna footprint and has three variable parameters: the number of sources N, the amplitude (power) of the individual RFI sources A, and the duty cycle of the individual RFI sources d. Based on the RFI brightness-temperature contribution observed during the SMAPVEX campaign, an exponential distribution has been used for amplitude. A bimodal distribution has been used for the duty cycle to account for both radar-type low duty-cycle signals and communicationlike CW signals. The fraction of low to high duty-cycle sources has been a variable parameter in the model.

Based on simulation results, it has been noted that the kurtosis algorithm has been impacted by central-limit conditions due to multiple sources. When most or all of the sources are of low duty-cycle, the kurtosis value converges toward three more slowly than when high duty-cycle sources are present. This indicates that a larger fraction of low duty-cycle RFI sources is required within the antenna footprint before the kurtosis detector is blind to RFI. In most cases such as SMAP, the pulse detection algorithm is applied along with the kurtosis detector that can detect high-power spikes due to multiple RFI sources. Multiple low-power communication sources such as Wi-Fi might pose a problem for radiometric measurements if they are undetectable by both algorithms.

The validity of the new RFI model and the behavior of kurtosis have been experimentally confirmed using a bench-top radiometer with a digital back end capable of measuring higher order moments of the signal. Results clearly have indicated that kurtosis is blind to high-power RFI due to the presence of multiple sources. If all of the RFI sources are high duty-cycle signals, results indicate that anywhere from 14 to 40 sources are required for the kurtosis algorithm to be blind to an RFI source above 1000 K. Thus, the new RFI model offers a possible explanation of observed high-power RFI sources not detected by the kurtosis algorithm.

Appendix

The characteristic function of a signal that is the sum of separate independent random variables is the product of the characteristic function of those random variables. The probability density can be found by taking the inverse Fourier transform of the resulting characteristic function. In order to calculate the pdf of thermal noise with multiple pulsed-sinusoidal RFI signals, the characteristic functions of the individual components are obtained and then multiplied together. The characteristic

function of a normal pdf is well known [30] and is shown as follows:

$$\varphi_n(u) = e^{-\frac{\sigma^2 u^2}{2}} \tag{9}$$

where σ is the standard deviation of a normally distributed function. The characteristic function of a pulsed sinusoid can be found as follows:

$$\begin{aligned}\varphi_{\mathrm{psi}}(u)_i &= \frac{1}{2\pi}\frac{1}{T}\int_0^{2\pi}\int_0^{T} e^{juA_i\cos(\omega_i t+\phi_i)\mathrm{rect}\left(\frac{t-t_0}{w_i}\right)}dt_0 d\phi \\ &= \frac{1}{2\pi}\int_0^{2\pi}\frac{1}{T}\left\{e^{juA_i\cos(\omega_i t+\phi_i)}w_i + T - w_i\right\}d\phi \\ &= \frac{1}{2\pi}\int_0^{2\pi}\left\{e^{juA_i(\omega_i t+\phi_i)}d_i + (1-d_i)\right\}d\phi \\ &= d_i J_0(A_i u) + (1-d_i)\end{aligned} \tag{10}$$

where J_0 is a Bessel function of the zeroth order, A_i is the amplitude of the RFI source, ω_l is the radian frequency, ϕ_l is the phase shift, t_0 represents the center of the on pulse of the duty cycle, w_i is the width of the on pulse, and T is the integration period. The ratio $(d_i = w_i/T)$ represents the duty cycle of the RFI source.

The total characteristic function is obtained by taking the product of (9) and (10) and is given by

$$\varphi_T(u) = \varphi_n(u)\prod_{i=1}^{N}\varphi_{\mathrm{psi}}(u)_i \tag{11}$$

where N is the total number of RFI sources. The probability density function $f(t)$ is the inverse Fourier transform of the characteristic function earlier.

REFERENCES

[1] E. G. Njoku, P. Ashcroft, T. K. Chan, and L. Li, "Global survey and statistics of radio-frequency interference in AMSR-E land observations," *IEEE Trans. Geosci. Remote Sens.*, vol. 43, no. 5, pp. 938–947, May 2005.

[2] L. Li, P. W. Gaiser, M. H. Bettenhausen, and W. Johnston, "WindSat radio-frequency interference signature and its identification over land and ocean," *IEEE Trans. Geosci. Remote Sens.*, vol. 44, no. 3, pp. 530–539, Mar. 2006.

[3] L. Li, E. G. Njoku, E. Im, P. S. Chang, and K. S. Germain, "A preliminary survey of radio-frequency interference over the U.S. in Aqua AMSR-E data," *IEEE Trans. Geosci. Remote Sens.*, vol. 42, no. 2, pp. 380–390, Feb. 2004.

[4] S. W. Ellingson and J. T. Johnson, "A polarimetric survey of radio-frequency interference in C- and X-bands in the continental United States using WindSat radiometry," *IEEE Trans. Geosci. Remote Sens.*, vol. 44, no. 3, pp. 540–548, Mar. 2006.

[5] S. Curry, M. Ahlers, H. Elliot, S. Gross, D. McKague, S. Misra, J. Puckett, and C. Ruf, "K-band radio frequency interference survey of Southeastern Michigan," in *Proc. IGARSS*, 2010, pp. 2486–2489.

[6] D. M. Le Vine, "ESTAR experience with RFI at L-band and implications for future passive microwave remote sensing from space," in *Proc. IGARSS*, 2002, vol. 2, pp. 847–849.

[7] J. Piepmeier and F. Pellerano, "Mitigation of terrestrial radar interference in L-band spaceborne microwave radiometers," in *Proc. IGARSS*, 2006, pp. 2292–2296.

[8] N. Skou, S. Misra, J. E. Balling, S. S. Kristensen, and S. S. Søbjærg, "L-band RFI as experienced during airborne campaigns in preparation for SMOS," *IEEE Trans. Geosci. Remote Sens.*, vol. 48, no. 3, pp. 1398–1407, Mar. 2010.

[9] S. Misra, S. S. Kristensen, S. S. Søbjærg, and N. Skou, "CoSMOS: Performance of kurtosis algorithm for radio frequency interference detection and mitigation," in *Proc. IGARSS*, 2007, pp. 2714–2717.

[10] C. S. Ruf, S. M. Gross, and S. Misra, "RFI detection and mitigation for microwave radiometry with an agile digital detector," *IEEE Trans. Geosci. Remote Sens.*, vol. 44, no. 3, pp. 694–706, Mar. 2006.

[11] S. Misra and C. S. Ruf, "Detection of radio-frequency interference for the Aquarius radiometer," *IEEE Trans. Geosci. Remote Sens.*, vol. 46, no. 10, pp. 3123–3128, Oct. 2008.

[12] National Research Council, Earth Science and Applications From Space: National Imperatives for the Next Decade and Beyond, Washington, DC, 2007.

[13] D. Bradley, C. Brambora, M. E. Wong, L. Miles, D. Durachka, B. Farmer, P. Mohammed, J. Piepmeier, J. Medeiros, N. Martin, and R. Garcia, "Radio-frequency interference (RFI) mitigation for the soil moisture active/passive (SMAP) radiometer," in *Proc. IGARSS*, 2010, pp. 2015–2018.

[14] S. Misra, C. Ruf, and R. D. De Roo, "Agile digital detector for RFI mitigation," in *Proc. IEEE MicroRad*, 2006, pp. 66–69.

[15] B. Guner, N. Niamsuwan, and J. T. Johnson, "Performance study of a cross-frequency detection algorithm for pulsed sinusoidal RFI in microwave radiometry," *IEEE Trans. Geosci. Remote Sens.*, vol. 48, no. 7, pp. 2899–2908, Jul. 2010.

[16] A. Camps, J. Gourrion, J. M. Tarongi, A. Gutierrez, J. Barbosa, and R. Castro, "RFI analysis in SMOS imagery," in *Proc. IGARSS*, 2010, pp. 2007–2010.

[17] S. Misra, R. De Roo, and C. Ruf, "Evaluation of the kurtosis algorithm in detecting radio frequency interference from multiple sources," in *Proc. IGARSS*, 2010, pp. 2019–2022.

[18] W. J. Wilson, S. H. Yueh, S. J. Dinardo, S. L. Chazanoff, A. Kitiyakara, F. K. Li, and Y. Rahmat-Samii, "Passive active L- and S-band (PALS) microwave sensor for ocean salinity and soil moisture measurements," *IEEE Trans. Geosci. Remote Sens.*, vol. 39, no. 5, pp. 1039–1048, May 2001.

[19] N. Niamsuwan, B. Guner, and J. Johnson, "Observations of an ARSR system in Canton, MI with the L-band interference suppressing radiometer," in *Proc. IGARSS*, 2006, pp. 2285–2288.

[20] J. R. Piepmeier, P. N. Mohammed, and J. J. Knuble, "A double detector for RFI mitigation in microwave radiometers," *IEEE Trans. Geosci. Remote Sens.*, vol. 46, no. 2, pp. 458–465, Feb. 2008.

[21] S. Misra, P. N. Mohammed, B. Guner, C. S. Ruf, J. R. Piepmeier, and J. T. Johnson, "Microwave radiometer radio-frequency interference detection algorithms: A comparative study," *IEEE Trans. Geosci. Remote Sens.*, vol. 47, no. 11, pp. 3742–3754, Nov. 2009.

[22] R. D. De Roo, S. Misra, and C. S. Ruf, "Sensitivity of the kurtosis statistic as a detector of pulsed sinusoidal RFI," *IEEE Trans. Geosci. Remote Sens.*, vol. 45, no. 7, pp. 1938–1946, Jul. 2007.

[23] R. D. De Roo and S. Misra, "A moment ratio RFI detection algorithm that can detect pulsed sinusoids of any duty cycle," *IEEE Geosci. Remote Sens. Lett.*, vol. 7, no. 3, pp. 606–610, Jul. 2010.

[24] S. Misra and C. Ruf, "Inversion algorithm for estimating radio frequency interference characteristics based on kurtosis measurements," in *Proc. IGARSS*, 2009, pp. II-162–II-165.

[25] S. Misra, C. Ruf, and R. Kroodsma, "Detectability of radio frequency interference due to spread spectrum communication signals using the kurtosis algorithm," in *Proc. IGARSS*, 2008, pp. II-335–II-338.

[26] J. Park, J. T. Johnson, N. Majurec, N. Niamsuwan, J. R. Piepmeier, P. N. Mohammed, C. S. Ruf, S. Misra, S. H. Yueh, and S. J. Dinardo, "Airborne L-band radio frequency interference observations from the SMAPVEX08 campaign and associated flights," *IEEE Trans. Geosci. Remote Sens.*, vol. 49, no. 9, pp. 3359–3370, Sep. 2011.

[27] S. O. Rice, "Statistical properties of a sine wave plus random noise," *Bell Syst. Tech. J.*, vol. 27, pp. 109–157, Jan. 1948.

[28] "Interference criteria for satellite passive remote sensing," International Telecommunications Union, Geneva, Switzerland, ITU-R RS.1029-2, 2003.

[29] C. Ruf and S. Gross, "Digital radiometers for earth science," in *Proc. IEEE MTT-S Int.*, 2010, pp. 828–831.

[30] M. G. Kendall, A. Stuart, J. K. Ord, S. F. Arnold, and A. O'Hagan, *Kendall's Advanced Theory of Statistics*, 6th ed. London, U.K.: Halsted Press, 1994.

[31] N. Skou, J. Balling, S. S. Søbjærg, and S. S. Kristensend, "Surveys and analysis of RFI in the SMOS context," in *Proc. IGARSS*, Jul. 2010, pp. 2011–2014.



Sidharth Misra (S'06–M'11) received the B.E. degree in electronics and communication engineering from the Nirma Institute of Technology, Gujarat University, Ahmedabad, India, in 2004, the M.S. degree in electrical engineering and computer science—signal processing—from the University of Michigan, Ann Arbor, in 2006, and the Ph.D. degree from the University of Michigan, in 2011.

He was a Research Engineer with the Space Physics Research Laboratory, University of Michigan, where he worked on the analysis and implementation of the agile digital receiver for RFI mitigation. He was a Research Assistant with the Danish National Space Center, Technical University of Denmark (DTU), Kgs. Lyngby, Denmark. He was also with the Space Applications Center, Indian Space Research Organization, Ahmedabad. He is currently with the Microwave Systems Technology Group, Jet Propulsion Laboratory, Pasadena, CA. He has many publications in the field of radio frequency interference detection and mitigation. He is currently working on the Aquarius radiometer calibration, as well as TOPography EXperiment (TOPEX) geophysical data record reprocessing. His research interests involve microwave radiometry, signal detection and estimation, and coastal altimetry.

Dr. Misra is the recipient of the International Geoscience and Remote Sensing Symposium 2006 Symposium Prize Paper Award and the Mikio Takagi Award at the IGARSS 2009 student prize paper competition.



Roger D. De Roo (S'88–M'96) received the B.S. degree in letters and engineering from Calvin College, Grand Rapids, MI, in 1986 and the B.S.E., M.S.E., and Ph.D. degrees in electrical engineering from the University of Michigan, Ann Arbor, in 1986, 1989, and 1996, respectively. His dissertation topic was on the modeling and measurement of bistatic scattering of electromagnetic waves from rough dielectric surfaces.

From 1996 to 2000, he was a Research Fellow with the Radiation Laboratory, Department of Electrical Engineering and Computer Science, University of Michigan, where he investigated the modeling and simulation of millimeter-wave backscattering phenomenology of terrain at near-grazing incidence. He is currently an Assistant Research Scientist and Lecturer with the Department of Atmospheric, Oceanic, and Space Sciences, University of Michigan. He has supervised the fabrication of numerous dual-polarization microcontroller-based microwave radiometers. His current research interests include digital correlating radiometer technology development, including radio frequency interference mitigation, and inversion of geophysical parameters such as soil moisture, snow water content, and vegetation parameters from radar and radiometric signatures of terrain.



Christopher S. Ruf (S'85–M'87–SM'92–F'01) received the B.A. degree in physics from Reed College, Portland, OR, and the Ph.D. degree in electrical and computer engineering from the University of Massachusetts, Amherst.

In 2000, he was a Guest Professor with the Technical University of Denmark (DTU), Lyngby, Denmark. He is currently a Professor of atmospheric, oceanic and space sciences; a Professor of electrical engineering and computer science; and the Director of the Space Physics Research Laboratory with the University of Michigan, Ann Arbor. He has been previously with Intel Corporation, Hughes Space and Communication, the National Aeronautics and Space Administration (NASA) Jet Propulsion Laboratory, Pasadena, CA, and Pennsylvania State University, University Park. He has published in the areas of microwave-radiometer satellite calibration, sensor and technology development, and atmospheric, oceanic, land surface, and cryosphere geophysical retrieval algorithms.He has served on the editorial boards of the American Geophysical Union (AGU) *Radio Science* and the American Meteorological Society (AMS) *Journal of Atmospheric and Oceanic Technology*.

Dr. Ruf is a member of AGU, AMS, and Commission F of the Union Radio Scientifique Internationale. He was the recipient of three NASA Certificates of Recognition and four NASA Group Achievement Awards, as well as the 1997 TRANSACTIONS ON GEOSCIENCE AND REMOTE SENSING (TGRS) Prize Paper Award, the 1999 IEEE Resnik Technical Field Award, and the 2006 International Geoscience and Remote Sensing Symposium Prize Paper Award. He has also served on the editorial board of the IEEE TGRS, of which he is currently the Editor-in-Chief.